Smart High-κ Nanodielectrics Using Solid Supported Polyoxometalate-Rich Nanostructures

Chiara Musumeci,[¶,†] Mali H. Rosnes,[¶,‡] Filippo Giannazzo,[§] Mark D. Symes,[‡] Leroy Cronin,[‡,*] and Bruno Pignataro[⊥,*]

[†]Superlab-Consorzio Catania Ricerche, Stradale Primosole 50, 95121 Catania, Italy, [‡]School of Chemistry, WestCHEM, University of Glasgow, Glasgow, G12 8QQ, United Kingdom, [§]CNR-IMM, Strada VIII, 5, Zona Industriale, 95121, Catania, Italy, and [⊥]Dipartimento di Chimica "S. Cannizzaro", Università di Palermo, V.le delle Scienze 90128 Palermo, Italy. [¶]These authors contributed equally to this publication.

ABSTRACT

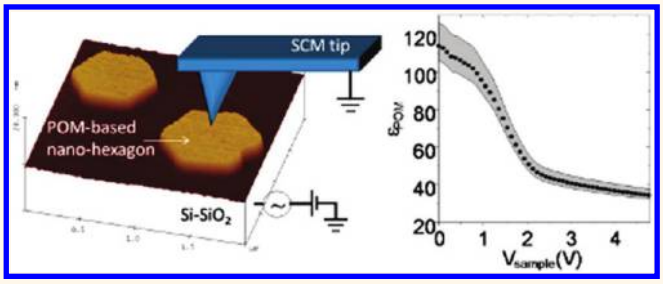

Utilizing Langmuir–Blodgett deposition and scanning probe microscopy, we have investigated the extent to which cations alter the self-assembly processes of hybrid polyoxometalates (POMs) on surfaces. The well-defined 2D hexagonal nanostructures obtained were extensively characterized and their properties were studied, and this has revealed fascinating dielectric behavior and reversible capacitive properties. The nanostructures are extremely stable under ambient conditions, and yet exhibit fascinating self-patterning upon heating. These findings present POMs as effective smart nanodielectrics and open up a new field for future POM applications.

KEYWORDS: polyoxometalate · high-κ nanodielectrics · smart materials · self-assembly · cation exchange · nanostructures

Polyoxometalates (POMs) are complex metal oxide molecules of growing interest due to their wide redox, photochemical, and catalytic properties.[1−3] The potential for these compounds to be used in functional devices has revealed the need for further investigation of their self-assembly and organization in the solid state and on solid substrates. In the past, the major studies in this respect have been mainly directed toward the fabrication of layered architectures, obtained by physical absorption, covalent attachment,[4,5] or by sequential grafting of oppositely charged polyelectrolytes onto planar substrates.[6] Only a very few examples[7,8] have been directed at the self-assembly on surfaces of this class of molecules. Recently, we focused our attention on the control of the physical and chemical parameters guiding the self-assembly and the self-organization of POMs on solid surfaces by solution processes.[9] We have demonstrated that by simply employing drop-casting deposition it is possible to induce the formation of architectures with a wide variety of shapes and dimensionalities as a function of different parameters, such as the structure of the cluster, the nature of its functionalization, the solution concentration, and thermal treatment of the film. Among the different POMs, the investigation of the self-assembly of hybrid organic–inorganic POMs is of immense interest because of the wide range of organic moieties with various functions that can be attached to, or associated with, the inorganic core.[10,11] The combined use of Langmuir–Blodgett deposition (LB) and scanning probe microscopy (SPM) techniques is very useful for investigating molecular self-assembly at the nanoscale.[12−15] There are several publications reporting the incorporation of POMs into the microspaces of LB films,[16−18] and LB deposition has been largely employed to build up multilayered films of POMs.[19,20] Recently we reported how, by utilizing the LB technique, hybrid organic–inorganic polyoxometalates can form nanoscopic fibrils at the air–water interface, and how the organic ligands involved change the structures obtained.[21] Herein we focus our attention on a symmetric Mn–Anderson having identical C9 alkyl ligands on either side of the cluster $[(MnMo_6O_{18})((OCH_2)_3C-C_9H_{17})_2]^{3-}$, compound **1**, and show how the nature of the countercation plays a crucial role in the self-assembly process. In a previous study, compound **1** gave no regular structures at the

* Address correspondence to bruno.pignataro@unipa.it, Lee.Cronin@glasgow.ac.uk.

Received for review October 3, 2011 and accepted November 8, 2011.

Published online November 08, 2011
10.1021/nn2037797

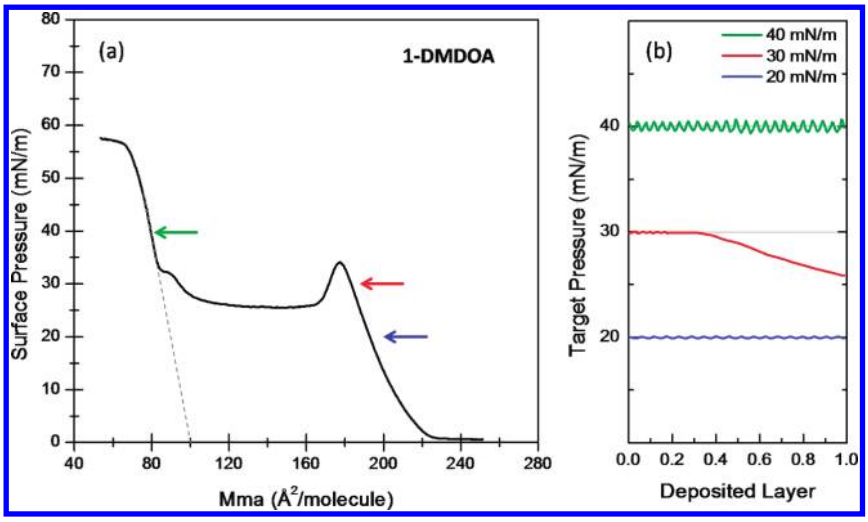

Figure 1. (a) Surface pressure *versus* mean molecular area isotherm, obtained at 25 °C, for 1-DMDOA. The dotted line extrapolates the limit area. (b) Surface pressure trends during the vertical deposition onto mica substrates.

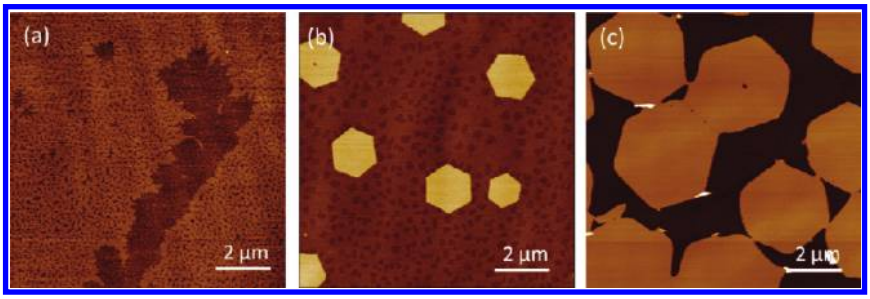

Figure 2. SFM images showing the morphology of 1-DMDOA deposited onto mica at target pressures of 20 (a), 30 (b), and 40 (c) mN m^{-1}. The *z* scale is 3 nm for panel a and 10 nm for panels b and c.

air–water interface with tetrabutylammonium (TBA) as the countercation.[21] Here we show that by exchanging the cation from TBA to dioctadecyldimethylammonium (DMDOA),[22] the resulting hybrid **1-DMDOA** gives rise to well-defined 2D hexagonal nanostructures showing high-κ dielectric behavior along with reversible capacitive properties.

RESULTS AND DISCUSSION

The Langmuir isotherm of **1-DMDOA** at the air–water interface is shown in Figure 1a. The surface pressure *versus* mean molecular area plot was obtained at 25 °C by taking a 10 μL aliquot of a 5 mg/mL solution of **1-DMDOA** (in 1:1 $CH_3CN/CHCl_3$) and spreading this onto the water subphase.

The plot shows regions with various shapes and slopes corresponding to the formation of different phases of the film at the air–water interface under barrier compression. A first transition from a "gas-like" phase to a condensed phase with a slope of −1.08 mN m^{-1} Å^{-2} is observed at a mean molecular area of 225 Å^2. Then at a molecular area of about 180 Å^2 with a pressure of about 35 mN m^{-1} the curve exhibits a transition point where the surface pressure starts to decrease, observed as a positive slope. This implies a molecular loss from the 2D compact phase into the water subphase. Subsequently, a steady pressure of 28 mN m^{-1} is observed during contraction of the molecular area from around 160 to 100 Å^2. The pressure then increases (with a slope of about −0.4 mN m^{-1} Å^{-2}) to a kink transition step at 30 mN m^{-1} (around 80 Å^2), after which the gradient of the curve becomes steeper (now −2.04 mN m^{-1} Å^{-2}), indicating the formation of a rigid "solid-like" phase. The surface pressure was monitored during the upstroke deposition and the value *versus* time plot is reported in Figure 1b. The pressure variation during deposition at 30 mN m^{-1} suggests that interesting molecular rearrangement phenomena are occurring near this transition point.

To observe in detail the structures induced by the self-assembly process at the air–water interface, different film transfer experiments onto solid substrates were carried out at 20, 30, and 40 mN m^{-1}, corresponding to the three diverse regions of the curves shown in Figure 1a,b; the first condensed phase (in blue); the crossover point (in red); and the final solid-like phase (in green), respectively. The morphologies of the transferred films are shown in the SFM images of Figure 2.

At the target pressure of 20 mN m^{-1} (Figure 2a) a "liquid-condensed" layer less than 1 nm thick is

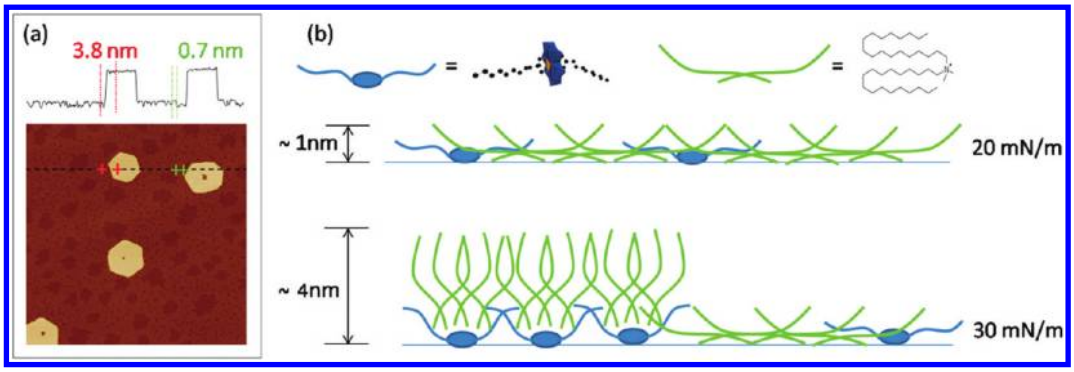

Figure 3. (a) Section profile showing the thickness of the hexagonal nanostructures and of the thin layer underneath. (b) Cartoon showing the possible molecular orientation during the transfer at 20 and 30 mN m^{-1} from the air−water interface.

observed. This thickness is consistent with molecules lying flat over the solid surface. At 30 mN m^{-1}, close to the crossover point, well-defined crystalline hexagonal nanostructures are observed together with the surrounding "liquid-condensed" layer (Figure 2b). Under these conditions the hexagonal aggregates are randomly spread over the substrate surface with a density of about 0.04 hexagons/μm^2, a projected area of 1.60 ± 0.1 μm^2 per hexagon and a thickness of 3.78 ± 0.46 nm. Finally at a pressure of 40 mN m^{-1}, very large hexagonal structures characterized by an average projected area of 10.1 ± 1.1 μm^2, a thickness of 3.70 ± 0.70 nm and a density of 0.05 hexagons/μm^2 are found. In particular, SFM shows that the hexagons are typically touching each other, with the thin liquid-condensed phase filling in the free-space in between the hexagons (Figure 2c). The formation of the hexagonal aggregates arises from the reorganization of a liquid-condensed phase whereby **1-DMDOA** self-assembles *via* van der Waals interactions between the alkyl chains on the DMDOA cations and the C9 chains on the inorganic anions (Figure 3b). Note that whereas DMDOA shows a +1 charge, the Mn−Anderson clusters are characterized by a −3 charge, so that on average each anion is associated with three cations. The pressure decrease at the transition point is in agreement with a film reorganization where the DMDOA molecules stack on top of the anionic C9−Mn−Anderson clusters, such that hydrophobic−hydrophobic interactions between the organic chains are maximized (Figure 3b). This self-assembly process thus involves the nucleation of hexagons, which then grow by the addition of molecules from the liquid-condensed thin layer. In this process, DMDOA molecules probably assemble on top of the relatively large C9−Mn−Anderson clusters (three DMDOA molecules per cluster in order to maintain charge balance). This configuration is indeed in close agreement with the measured SFM height of the hexagonal structures, that is, an average thickness of 3.8 nm (Figure 3a), closely resembles the size of the anionic cluster (about 1 nm), with the amphiphilic cation on top, in a stretched configuration (about 2.5 nm, from crystallographic data[23]). Accordingly, the formation of the hexagonal crystals would arise by the cooperative action of the van der Waals forces between the hydrophobic tails and the electrostatic interactions of the charged moieties. In contrast, although the transfer at 40 mN m^{-1} is slightly noisy (Figure 1b), the pressure remains constant due to the fact that hexagons formed are now large enough to transfer without loss of film rigidity; that is, the hexagons are so large they now behave like a continuous monomolecular layer (compare hexagon coverage in Figure 2 panels b and c).

In a recent paper, Misdrahi *et al*. demonstrated that functionalization with organic substituents can control the behavior of POM-organic hybrids at the air−water interface during LB deposition,[24] and that the different phases have a large range of molecular areas as a result of the size of the POM hybrid. In our case, the solid state molecular area (about 80 $Å^2$) is in agreement with our model whereby the POM cluster size plays a major role: the extrapolated limit area at zero pressure (about 100 $Å^2$) is consistent with the large molecular area of **1-DMDOA**, and the long transition region from roughly 160 to 100 $Å^2$ is in agreement with the amphiphilic anion−cation reorganization at the air−water interface.

Interestingly, when **1-DMDOA** is transferred under the same conditions onto a Si substrate (p-type doped, 10^{18} cm^{-3}, cleaned by oxygen plasma and still with its native thin oxide SiO_2), no liquid-condensed phase is visible surrounding the hexagons, indicating a different mode of interaction of the free molecules with this substrate during deposition (see Figure 4a,b).

The hexagonal nanostructures formed on Si were characterized by torsional resonant conductive atomic force microscopy (TRCAFM) and scanning capacitance microscopy (SCM). TRCAFM experiments were performed with a Pt/Ir-coated Si tip by applying increasing positive bias to the doped Si substrate (electron injection to the substrate from the tip) and measuring the transversal current flowing from the underside of the sample to the grounded nanometric tip. Typical images of the surface morphology measured in torsion

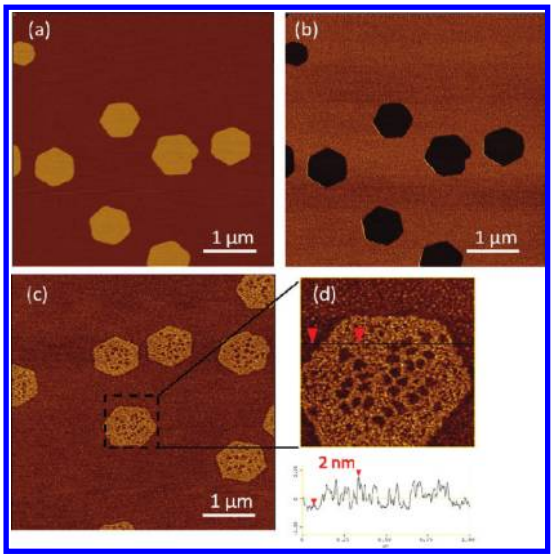

Figure 4. 1-DMDOA deposited onto native silicon oxide, before (a,b) and after (c,d) thermal treatment at 270 °C for 4 h. In contrast to Supporting Information, Figure S7a, a very definite color contrast is visible on the phase image (4b) as an indication of different viscoelastic and adhesion properties, clearly showing that there are no free molecules present on this substrate beyond the hexagonal nanostructures. The hexagons are about 4 nm tall, as in the case of the mica substrate. After the thermal treatment the hexagonal shapes are still visible but they are holed and their thickness is reduced to about 2 nm (see cross-section in 4d).

resonant mode and of the corresponding current map are reported in Figure 5 panels a and b, respectively. When a bias higher than 6 V is applied, a contrast appears in the current map (femtoAmpere scale), and the hexagons appear as darker in color than the background. This means that a lower current flows through the hexagon/SiO_2/Si stacks than through naked SiO_2/Si, suggesting that the hexagonal aggregates have insulating properties. Applied voltages larger than 8 V lead to the destruction of the hexagons, with transport of material from the hexagons to the tip. No contrast in the current map or any damage is visible when a negative voltage is applied (see Supporting Information). This supports our theory, depicted in Figure 3b, that the DMDOA cations are in the upper layer of the hexagonal nanostructures, and hence more easily removed by the tip through electrostatic interactions when the tip is anodically biased.

Figure 5 panels c and d report the SCM measurements comparing the capacitance behavior of the native silicon oxide on top of the silicon substrate (SiO_2/Si) (Figure 5c) with that of the **1-DMDOA** hexagonal nanostructures on top of SiO_2/Si (**1-DMDOA**/SiO_2/Si) (Figure 5d). In both cases the d*C*/d*V* curves were acquired with a V_{sample} ramp from negative to positive values (black curves) and from positive to negative values (red curves). Intriguingly, Figure 5d shows that when a sample bias of about 1.8 V (electron injection from the tip) is applied, a peak for **1-DMDOA**/SiO_2/Si is observed. Such a capacitance change is likely associated with a structural change of the POM system. This kind of change is clearly reversible, since it is observed both for the voltage ramp-up and during the voltage ramp-down.

Similar behavior to that seen on the nanoscale using such SCM studies in the solid state is also observed by macroscopic cyclic voltammetry measurements in solution (Figure 6). In the anodic direction, cyclic voltammetry shows a pseudoreversible redox wave centered around +0.2 V *versus* ferrocene, which corresponds to the Mn^{3+}/Mn^{4+} redox couple, in agreement with previous reports on related compounds.[25] The peak separation between the oxidation and reduction peaks is in the region of 400 mV, suggesting slow kinetics for this redox process. In the cathodic direction, compound **1** has a single reversible, well-behaved redox wave at −1.2 V (*vs* ferrocene) which corresponds to the Mn^{2+}/Mn^{3+} couple. The large peak separation between the reduction and reoxidation waves (around 550 mV), again suggests that this process is also slow on the time scale of the experiment (0.1 V s^{-1}), implying geometrical changes at the Mn center during reduction. This is consistent with the solid-state SCM data. Accordingly, SCM suggests that electron injection into the nanostructures might be accompanied by structural changes on the nanoscale. Although CV data are collected in solution, the above findings suggest that this effect might be ascribed to the reduction of Mn^{3+} to Mn^{2+} as a result of geometrical changes. These structural changes of the POM cluster would give rise to a change in the capacitance of the **1-DMDOA** hexagonal nanostructures, and ultimately to a change in its "effective" dielectric constant ($\varepsilon_{\mathbf{1}\text{-DMDOA}}$). Figure 5e reports $\varepsilon_{\mathbf{1}\text{-DMDOA}}$ *versus* the applied bias calculated for the hexagonal nanostructures by using the SCM measurements shown in Figure 5c,d. $\varepsilon_{\mathbf{1}\text{-DMDOA}}$ has been evaluated considering the **1-DMDOA** hexagonal nanostructures as a dielectric layer with thickness $t_{\mathbf{1}\text{-DMDOA}} \approx 3.8$ nm and capacitance per unit area $C_{\mathbf{1}\text{-DMDOA}} = \varepsilon_0\varepsilon_{\mathbf{1}\text{-DMDOA}}/t_{\mathbf{1}\text{-DMDOA}}$, where ε_0 is the vacuum dielectric constant. The capacitance of the **1-DMDOA**/SiO_2/Si system can therefore be described as the series combination of the **1-DMDOA** hexagonal nanostructures capacitance and the SiO_2/Si capacitance. The latter capacitance is independently measured when the tip is placed on naked SiO_2/Si. Further details on this calculation are reported in the Supporting Information. Interestingly, Figure 5e shows that modulation of the sample bias from 1 to 2 V leads to a sharp decrease in the value of $\varepsilon_{\mathbf{1}\text{-DMDOA}}$ from about 115 ± 10 to about 36 ± 3, which correlates well with the structural changes which CV suggests occur during redox processes at the Mn center. The error in the estimation of $\varepsilon_{\mathbf{1}\text{-DMDOA}}$ by this comparative capacitance method in the range of sample bias considered is represented by the gray shaded area in Figure 5e. In agreement with CV measurements, this behavior has

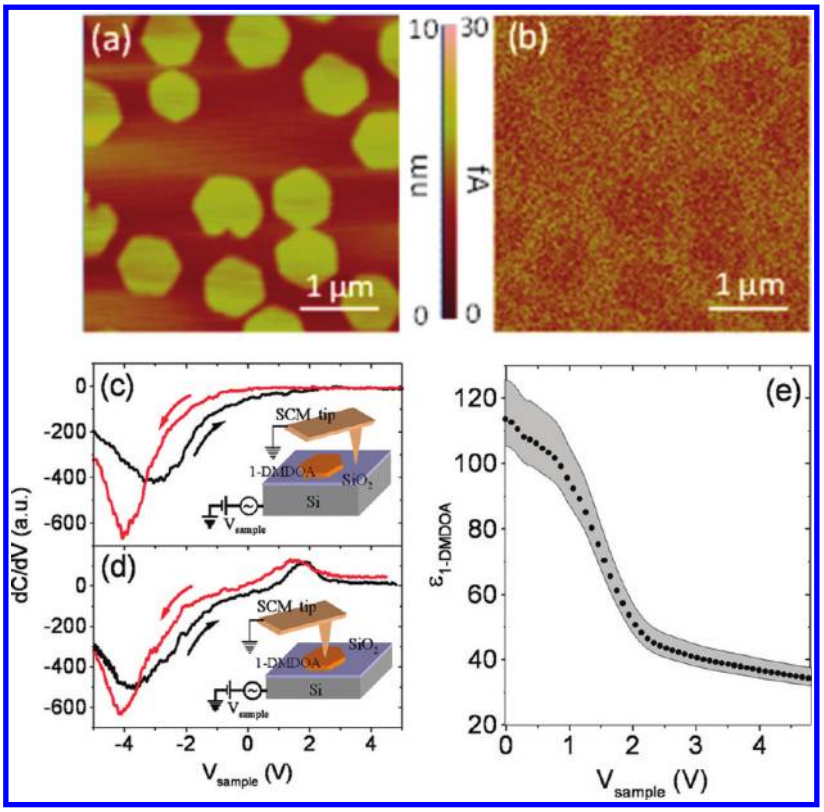

Figure 5. Surface morphology measured in torsional resonant mode (a) and corresponding current map (b) of 1-DMDOA deposited onto Si with its thin native oxide layer (thickness 1.5 ± 0.3 nm). Derivative of capacitance with respect to voltage (d*C*/d*V*) *versus* sample dc bias (V_{sample}) measured by SCM when the tip is in contact with SiO_2 (c) and with 1-DMDOA/SiO_2 (d). d*C*/d*V* curves were acquired with a V_{sample} ramp from negative to positive values (black curve) and from positive to negative values (red curve). (e) $\varepsilon_{1\text{-DMDOA}}$ *versus* the applied bias calculated for the hexagonal nanostructures by using the SCM measurements shown in Figures 5c,d; the error is shown in gray.

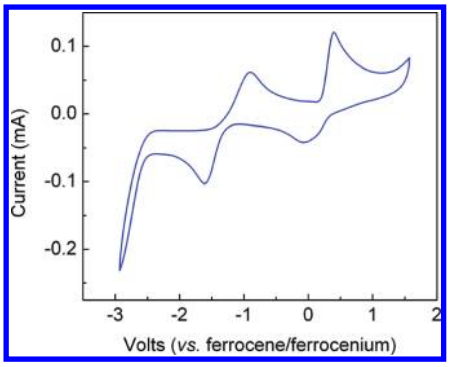

Figure 6. The cyclic voltammetry of compound 1 in 0.1 M TBA-BF_4/CH_3CN at 0.1 V/s using a 3 mm diameter glassy carbon working electrode shows a pseudoreversible wave centered around +0.2 V which corresponds to the Mn^{3+}/Mn^{4+} redox couple. In the cathodic direction, compound 1 has a single reversible, well-behaved redox wave at −1.2 V (vs ferrocene) which corresponds to the Mn^{2+}/Mn^{3+} couple.

been found to be quite reversible under the cyclic scan bias. Moreover, the values of $\varepsilon_{\mathbf{1}\text{-DMDOA}}$ are in the range of the high-κ dielectrics rendering such systems particularly attractive as smart nanodielectrics in emerging fields such as nano- and plastic-electronics or biological field effect transistors where the use of low voltages is required.[26] To date, different systems have been investigated for these functions, from metal oxides to polymers, from nanocomposites to self-assembled monolayers,[26] and so far high dielectric constant values similar to ours have been observed only for titano−oxide and titano−niobate nanofilms.[27,28]

To investigate the stability of the obtained nanostructures, we checked the samples by AFM again after a period of 6 months, without any observable changes. If however a sample of hexagonal nanostructures of **1-DMDOA** was heated up to 270 °C for 4 h, the properties of that sample changed dramatically. The height of the hexagons was observed to decrease from about 4 nm to about 2 nm, (compare Figure 4 panels a and c after the thermal treatment) and although the hexagonal nanostructures were still intact, multiple holes appeared throughout the structures. The samples were heated to 270 °C because thermogravimetric analysis (TGA) shows that **1-DMDOA** is stable up to roughly 250 °C (temperature gradient of 10 °C min^{-1}). Above that temperature the organic moieties of the compound start to decompose. The overall weight percentage lost up to 700 °C was found to be equal to the weight calculated for the three DMDOA cations associated with each anion of compound **1**, plus the two C9-chains which are attached to the Mn−Anderson core (see Supporting Information). This,

and the fact that the height of the hexagons is reduced upon heating, supports our theory regarding how compound **1** aligns on the substrate with the DMDOA cations arranged on top, forming the hexagonal nanostructures. Moreover, SCM measurements on these thermally treated hexagons show similar capacitance behavior to hexagons of **1-DMDOA** (see Supporting Information), further confirming that the smart dielectric properties are confined to the inorganic POM clusters. The role of the organic moieties thus appears to be to direct the formation of the hexagons.

CONCLUSIONS

In conclusion, the results presented here show how important the cations are to the formation and properties of hybrid organic–inorganic clusters on surfaces and this, together with our previous publication,[21] presents an important and valuable tool for design and control of self-assembly on surfaces by employing the correct combination of POM, organic ligand, and cation. Second, we have shown that the structures obtained are of high stability, and we can support our theories regarding the arrangement of **1-DMDOA** into hexagonal nanostructures based on studies of the transfer process, investigation of electronic behavior of the hexagons, and TGA analysis. We also found that upon heating, regular holes appear within the hexagonal nanostructures, and this is a unique example of self-patterning that could potentially be utilized as multiparallel nanoreactors. Finally, and most importantly, we have shown that the hexagonal POM-based nanostructures are effective smart nanodielectrics; their dielectric constant alters dramatically over a relatively small potential window and reaches values consistent with giant molecular polarizability.[28] Owing to the stability, high-κ properties, and modulation capability of these structures, as well as to their processability by solution techniques, these findings have great potential for novel supramolecular assemblies in emerging scientific and technological fields such as smart materials in plastics and hybrid (organic–inorganic) electronic devices. Important application fields may concern those of memories, capacitors, gate insulators, energy storage, field-effect transistors, and complementary logics or high-frequency modulation in communication devices, but also new possible avenues of research are possible in the fields of multiparallel nanoreactors and chemical or biological FET-sensors at low voltages.[29–31]

METHODS

Materials. All reagents and chemicals were supplied by Sigma-Aldrich Chemical Co. Ltd., and solvents were supplied by Fisher Chemicals, all used without further purification. The synthesis of the TBA salt of compound **1**, where TBA = tertbutylammonium bromide = $(N(C_4H_9)_4)$, has been published previously.[21]

Elemental Analysis. Carbon, nitrogen, and hydrogen content were determined by the microanalysis services within the Department of Chemistry, University of Glasgow using an EA 1110 CHNS, CE-440 Elemental Analyzer.

UV–Visible Spectroscopy. UV–vis spectra were all collected on a JASCO V-670 spectrophotometer.

Thermogravimetric Analysis (TGA). Thermogravimetric analysis was performed on a TA Instruments Q 500 ThermogravimetricAnalyzer under nitrogen flow at a typical heating rate of 10 °C min^{-1}.

NMR Spectroscopy. All NMR data were recorded on a Bruker Advance 400 MHz, ^{1}H NMR at 400 MHz in deuterated chloroform from Goss Scientific, at $T = 300$ K. All shifts are given in ppm and all coupling constants (J) are given in Hz.

Electrospray Mass Spectroscopic Measurements. All MS data were collected using a Q-trap, time-of-flight MS (MicroTOF-Q MS) instrument equipped with an electrospray (ESI) source supplied by BrukerDaltonics Ltd. All analyses were carried out at 180 °C in a small amount of dichloromethane in acetonitrile and collected in negative ion mode. The spectrometer was calibrated with the standard tune-mix to give a precision of *ca.* 1.5 ppm in the region of 500–3000 m/z.

Fourier-Transform Infrared (FT-IR) Spectroscopy. All spectra were recorded on a Shimadzu FTIR 8400S Fourier transformer infrared spectrophotometer. Wavenumbers ($\tilde{V}$) are given in cm^{-1}; intensities as denoted as w = weak, m = medium, s = strong, vs = very strong, sh = sharp, br = broad.

Synthesis of 1-DMDOA. The cation exchange was performed according to an adapted literature procedure.[22] $(N(C_4H_9)_4)_3[MnMo_6O_{18}((OCH_2)_3C–C_9H_{17})_2]$[21] (0.20 g, 9.5×10^{-5} mol) was dissolved in 15 mL of acetonitrile, and the solution was kept stirring for 30 min. It was then added dropwise to a clear solution of DMDOA·Br (0.60 g, 9.5×10^{-4} mol) in 15 mL of chloroform and 35 mL of acetonitrile. The reaction mixture was stirred for 30 min before the precipitate was collected by filtration. Any unreacted TBA salt of compound **1**, excess DMDOA·Br and TBA·Br were washed away with methanol, before the product was collected as a pale orange solid (0.14 g, 4.6×10^{-5} mol, 36%). Elemental analysis $[Mo_6Mn_1O_{24}N_3C_{140}H_{286}]$ (3026.35 g/mol), % found (calculated values in brackets): C, 55.54 (55.56); H, 9.59 (9.53); N, 1.32 (1.39). Characteristic IR bands: 2916 (s), 2847 (s), 1643 (w), 1466 (m), 1111 (w), 1018 (m), 926 (s), 648 (vs). ^{1}H NMR ($CDCl_3$, 400 MHz): δ 64.00–59.60 (br, m, 12H*), 8.25–7.45 (m, 4H), 5.90–5.70 (m, 2H), 5.01 (d, 2H, $^3J = 16.8$), 4.94 (d, 2H, $^3J = 9.7$), 3.60–2.85 (m, 30H), 2.10–1.95 (m, 4H), 1.85–1.55 (m, 12H), 1.55–1.04 (m, 200H), 0.87 (t, 18H, $^3J = 6.8$).

General Methods for Surface Techniques and Analysis: Langmuir–Blodgett Experiments. Langmuir–Blodgett deposition was performed on a KSV minitrough apparatus. Ultrapure Millipore filtered water with resistivity greater than 18.2 MΩ·cm was used as the subphase. The experiments were performed at a subphase temperature of 25 and 40 °C. Compound **1-DMDOA** was dissolved at concentrations of 5 mg/mL in a mixture of acetonitrile (Aldrich, 99.9%) and chloroform (Aldrich, 99.9%) with a volume ratio of 1:1. Drops of the above solutions were randomly spread over the aqueous subphase. After a few minutes the floating films were linearly compressed by two mobile barriers at a rate of 5 mm/min. Surface-pressure versus molecular-area isotherms were recorded by film balance measurement. The ultrathin film transfers were performed onto different substrates (mica, native silicon oxide and indium tin oxide on PEN (data not shown) by an upstroke operation (vertical transfer) at speed of 5 mm/min. The mica substrate was chosen to give a smooth surface to ensure higher quality images of the nanoscopic features by SFM microscopy. The LB layer deposited on mica was left to dry in air and successively observed by dynamic scanning force microscopy (SFM).

Scanning Force Microscopy. Both noncontact and intermittent-contact modes were employed for the morphological characterization of the transferred films by dynamic scanning force microscopy (SFM) through a Multimode NanoscopeIIIa (Digital Instruments) equipped with a phase extender apparatus and a Q-box module, and operating in air. Etched-silicon probes (pyramidal-shaped tip, nominal curvature 10 nm, nominal internal angle 35°) were used. During the scanning, the 125 μm-long cantilever, with a nominal spring constant in the range of 20−100 N/m, oscillated at its resonance frequency (~330 kHz). Height and phase images were collected by capturing 512 × 512 points in each scan and the scan rate was maintained below 1 line per second. During the imaging, temperature and humidity were about 25 °C and 40%, respectively.

Torsion Resonant Conductive Atomic Force Microscopy (TRCAFM). Both conventional contact mode conductive atomic force microscopy (CAFM) and torsional resonant conductive atomic force microscopy (TRCAFM) measurements were carried out on the samples. Contact mode CAFM caused a morphological degradation of the hexagonal structures. In contrast, TRCAFM allowed information regarding the nanostructures' conductivity to be obtained without severely damaging the hexagonal aggregates. Torsion resonant conductive AFM was performed with a Digital Dimension 3100 microscope with Nanoscope V electronics. Pt-coated Si tips with Pt/Ir-coated Si tips purchased by Nanosensors with 225 ± 10 μm-long cantilever and spring constant in the range 21−98 N/m were driven in torsional motion at a frequency of 1430 kHz. The torsion amplitude was used as the feedback signal to measure surface morphology. Current maps were measured by the CAFM sensor connected to the tip, when a dc bias is applied to the sample (V_{sample}).

Scanning Capacitance Microscopy. Scanning capacitance microscopy measurements were carried out with a Digital Dimension 3100 microscope with Nanoscope V electronics and the SCM module. Measurements were carried out in contact mode using Pt-coated Si. A dc bias ramp (V_{sample}) plus a small modulating bias (V_{ac}) with amplitude 100 mV and frequency 100 kHz was applied to the sample. The capacitance variations (dC/dV) induced by the modulating bias were measured by the SCM capacitance sensor connected to the tip.

Acknowledgment. L.C. thanks the EPSRC for funding and the Royal-Society Wolfson Foundation for a Merit Award, and M.H.R. and M.D.S. thank the University of Glasgow. B.P. acknowledges Italian MiUR (FIRB Futuro in Ricerca 2008, Laboratorio Pubblico-Privato PLAST_ICs) and the University of Palermo for funding.

Supporting Information Available: Full characterization of compound **1-DMDOA**; full methods and results for surface techniques and analysis; Langmuir−Blodgett experiments; scanning force microscopy, torsion resonant conductive atomic force microscopy (TRCAFM); scanning capacitance microscopy. This material is available free of charge *via* the Internet at http://pubs.acs.org.

REFERENCES AND NOTES

1. Long, D.-L.; Tsunashima, R.; Cronin, L. Polyoxometalates: Building Blocks for Functional Nanoscale Systems. *Angew. Chem., Int. Ed.* **2010**, *49*, 1736–1758.
2. Proust, A.; Thouvenot, R.; Gouzerh, P. Functionalization of Polyoxometalates: Towards Advanced Applications in Catalysis and Materials Science. *Chem. Commun.* **2008**, 1837–1852.
3. Ritchie, C.; Streb, C.; Thiel, J.; Mitchell, S. G.; Miras, H. N.; Long, D.-L.; Boyd, T.; Peacock, R. D.; McGlone, T.; Cronin, L. Reversible Redox Reactions in an Extended Polyoxometalate Framework Solid. *Angew. Chem., Int. Ed.* **2008**, *47*, 6881–6884.
4. Errington, R. J.; Petkar, S. S.; Horrocks, B. R.; Houlton, A.; Lie, L. H.; Patole, S. N. Covalent Immobilization of a TiW_5 Polyoxometalate on Derivatized Silicon Surfaces. *Angew. Chem., Int. Ed.* **2005**, *44*, 1254–1257.
5. Song, Y.-F.; McMillan, N.; Long, D.-L.; Kane, S.; Malm, J.; Riehle, M. O.; Pradeep, C. P.; Gadegaard, N.; Cronin, L. Micropatterned Surfaces with Covalently Grafted Unsymmetrical Polyoxometalate-Hybrid Clusters Lead to Selective Cell Adhesion. *J. Am. Chem. Soc.* **2009**, *131*, 1340–1341.
6. Li, M.; Jian, X. Synthesis and Electroluminescence Properties of Europium (III) Complexes with New Second Ligands. *Thin Solid Films* **2005**, *478*, 305–309.
7. Yan, Y.; Wang, H.; Li, B.; Hou, G.; Yin, Z.; Wu, L.; Yam, V. W. W. Smart Self-Assemblies Based on a Surfactant-Encapsulated Photoresponsive Polyoxometalate Complex. *Angew. Chem., Int. Ed.* **2010**, *49*, 9233–9236.
8. Nisar, A.; Lu, Y.; Wang, X. Assembling Polyoxometalate Clusters into Advanced Nanoarchitectures. *Chem. Mater.* **2010**, *22*, 3511–3518.
9. Musumeci, C.; Luzio, A.; Pradeep, C. P.; Miras, H. N.; Rosnes, M. H.; Song, Y.-F.; Long, D.-L.; Cronin, L.; Pignataro, B. Programmable Surface Architectures Derived from Hybrid Polyoxometalate-Based Clusters. *J. Phys. Chem. C* **2011**, *115*, 4446–4455.
10. Song, Y.-F.; Long, D.-L.; Cronin, L. Noncovalently Connected Frameworks with Nanoscale Channels Assembled from a Tethered Polyoxometalate−Pyrene Hybrid. *Angew. Chem., Int. Ed.* **2007**, *46*, 3900–3904.
11. Ritchie, C.; Burkholder, E. M.; Long, D.-L.; Adam, D.; Kögerler, P.; Cronin, L. Exploiting the Multifunctionality of Organocations in the Assembly of Hybrid Polyoxometalate Clusters and Networks. *Chem. Commun.* **2007**, 468–470.
12. Pignataro, B. Nanostructured Molecular Surfaces: Advances in Investigation and Patterning Tools. *J. Mater. Chem.* **2009**, *19*, 3338–3350.
13. Raudino, A.; Pignataro, B. Switching Direction of Laterally Ordered Monolayers Induced by Transfer Instability. *J. Phys. Chem. B* **2007**, *111*, 9189–9192.
14. Pignataro, B.; Sardone, L.; Marletta, G. Dynamic Scanning Force Microscopy Investigation of Nanostructured Spiral-like Domains in Langmuir−Blodgett monolayers. *Nanotechnology* **2003**, *14*, 245–249.
15. Fabiano, S.; Pignataro, B. Engineering 3D Ordered Molecular Thin Films by Nanoscale Control. *Phys. Chem. Chem. Phys.* **2010**, *12*, 14848–14860.
16. Wang, X. L.; Wang, Y. H.; Hu, C. W.; Wang, E. B. Fabrication of Photoluminescent Multibilayer Composite Films Consisting of a Rare-Earth-Containing Polyoxometalate $Na_9[EuW_{10}O_{36}]$ and Dimethyldioctadecylammonium Chloride. *Mater. Lett.* **2002**, *56*, 305–311.
17. Clemente-León, M.; Mingotaud, C.; Agricole, B.; Gómez-Garcia, C. J.; Coronado, E.; Delhaès, P. Application of the Langmuir−Blodgett Technique to Polyoxometalates: Towards New Magnetic Films. *Angew. Chem., Int. Ed.* **1997**, *36*, 1114–116.
18. Clemente-León, M.; Agricole, B.; Mingotaud, C.; Gómez-Garcia, C. J.; Coronado, E.; Delhaès, P. Toward New Organic/Inorganic Superlattices: Keggin Polyoxometalates in Langmuir and Langmuir−Blodgett Films. *Langmuir* **1997**, *13*, 2340–2347.
19. Clemente-León, M.; Coronado, E.; Soriano-Portillo, A.; Mingotaud, C.; Dominguez-Vera, J. M. Langmuir-Blodgett Films Based on Inorganic Molecular Complexes with Magnetic or Optical Properties. *Adv. Colloid Interface Sci.* **2005**, *116*, 193–203.
20. Clemente-León, M.; Coronado, E.; Gómez-Garcia, C. J.; Mingotaud, C.; Ravaine, S.; Romualdo-Torres, G.; Delhaès, P. Polyoxometalate Monolayers in Langmuir−Blodgett Films. *Chem.—Eur. J.* **2005**, *11*, 3979–3987.
21. Rosnes, M. H.; Musumeci, C.; Pradeep, C. P.; Mathieson, J. S.; Long, D.-L.; Song, Y.-F.; Pignataro, B.; Cogdell, R.; Cronin, L. Assembly of Modular Asymmetric Organic−Inorganic Polyoxometalate Hybrids into Anisotropic Nanostructures. *J. Am. Chem. Soc.* **2010**, *132*, 15490–15492.
22. Song, Y.-F.; McMillan, N.; Long, D.-L.; Thiel, J.; Ding, Y.; Chen, H.; Gadegaard, N.; Cronin, L. Design of Hydrophobic Polyoxometalate Hybrid Assemblies beyond Surfactant Encapsulation. *Chem.—Eur. J.* **2008**, *14*, 2349–2354.

23. Ito, T.; Sawada, K.; Yamase, T. Crystal Structure of Bis-(dimethyldioctadecylammonium) Hexamolybdate: A Molecular Model of Langmuir–Blodgett Films. *Chem. Lett.* **2003**, *32*, 938–939.
24. Misdrahi, M. F.; Wang, M.; Pradeep, C. P.; Li, F. Y.; Lydon, C.; Xu, L.; Cronin, L.; Liu, T. Amphiphilic Properties of Dumbbell-Shaped Inorganic–Organic–Inorganic Molecular Hybrid Materials in Solution and at an Interface. *Langmuir* **2011**, *27*, 9193–9202.
25. Allain, C.; Favette, S.; Chamoreau, L. M.; Vaissermann, J.; Ruhlmann, L.; Hasenknopf, B. Hybrid Organic–Inorganic Porphyrin–Polyoxometalate Complexes. *Eur. J. Inorg. Chem.* **2008**, 3433–3441.
26. Ortiz, R. P.; Facchetti, A.; Marks, T. J. High-*k* Organic, Inorganic, and Hybrid Dielectrics for Low-Voltage Organic Field-Effect Transistors. *Chem. Rev.* **2010**, *110*, 205–239.
27. Osada, M.; Akatsuka, K.; Ebina, Y.; Funakubo, H.; Kiguchi, T.; Takada, K.; Sasaki, T. Solution-Based Fabrication of High-κ Dielectric Nanofilms Using Titania Nanosheets as a Building Block. *Jpn. J. Appl. Phys.* **2007**, *46*, 6979–6983.
28. Osada, M.; Takanashi, G.; Li, B.-W.; Akatsuka, K.; Ebina, Y.; Ono, K.; Funakubo, H.; Takada, K.; Sasaki, T. Controlled Polarizability of One-Nanometer-Thick Oxide Nanosheets for Tailored, High-κ Nanodielectrics. *Adv. Funct. Mater.* **2011**, *21*, 3482–3487.
29. Ballato, A. In *Advances in Dielectric Ceramic Materials*; Nair, K. M., Bhalla, A. S., Eds.; The American Ceramic Society: Westerville, OH, 1998; pp 1–14.
30. Kingon, A. I.; Maria, J. P.; Streiffer, S. K. Alternative Dielectrics to Silicon Dioxide for Memory and Logic Devices. *Nature* **2000**, *406*, 1032–1038.
31. Cava, R. J. *J.* Dielectric Materials for Applications in Microwave Communications. *Mater. Chem.* **2001**, *11*, 54–62.